Title	Fast magnetic-field annihilation in the relativistic collisionless regime driven by two ultrashort high-intensity laser pulses
Author(s)	Gu Y. J., Klimo O., Kumar D., Liu Y., Singh S. K., Esirkepov T. Z., Bulanov S. V., Weber S., Korn G.
Citation	Physical Review E, 93(1), p.013203_1-013203_6
Text Version	Publisher's Version
URL	https://jopss.jaea.go.jp/search/servlet/search?5054686
DOI	https://doi.org/10.1103/PhysRevE.93.013203
Right	© 2016 The American Physical Society

Fast magnetic-field annihilation in the relativistic collisionless regime driven by two ultrashort high-intensity laser pulses

Y. J. Gu,[1,*] O. Klimo,[1,2] D. Kumar,[1] Y. Liu,[1] S. K. Singh,[1] T. Zh. Esirkepov,[3] S. V. Bulanov,[3] S. Weber,[1] and G. Korn[1]

[1]*Institute of Physics of the ASCR, ELI-Beamlines, Na Slovance 2, 18221 Prague, Czech Republic*

[2]*FNSPE, Czech Technical University in Prague, 11519 Prague, Czech Republic*

[3]*Kansai Photon Science Institute, Japan Atomic Energy Agency, 8-1-7 Umemidai, Kizugawa-shi, Kyoto 619-0215, Japan*

(Received 20 April 2015; revised manuscript received 18 September 2015; published 8 January 2016)

The magnetic quadrupole structure formation during the interaction of two ultrashort high power laser pulses with a collisionless plasma is demonstrated with 2.5-dimensional particle-in-cell simulations. The subsequent expansion of the quadrupole is accompanied by magnetic-field annihilation in the ultrarelativistic regime, when the magnetic field cannot be sustained by the plasma current. This results in a dominant contribution of the displacement current exciting a strong large scale electric field. This field leads to the conversion of magnetic energy into kinetic energy of accelerated electrons inside the thin current sheet.

DOI: 10.1103/PhysRevE.93.013203

I. INTRODUCTION

Generation of high energy particles in space and laboratory plasmas has been attracting a lot of attention for years. Magnetic reconnection [1] is one of the processes allowing the energy transfer from magnetic field into charged particles [2]. It plays a fundamental role in the magnetic confinement of thermonuclear plasma [3] and has been considered as a plausible mechanism for high energy charged particle generation in space plasmas [2,4–6]. This process is accompanied by a current sheet formation [1,7–9], where the oppositely directed magnetic fields annihilate. The magnetic-field annihilation has been investigated within the framework of dissipative magnetohydrodynamics (see Ref. [10] and literature cited therein). In ultrarelativistic plasma, it becomes principally different because the electron current has the upper limit [11]. Due to the relativistic constraint on the particle velocity (which never exceeds the speed of light in vacuum) the electric current can sustain only a limiting magnetic-field strength. Sometimes the corresponding regime is called "Syrovatskii's mechanism of charged particle acceleration," whereas S. I. Syrovatskii called it "dynamic dissipation of the magnetic field" [11].

The development of high power lasers [12] allows accessing new regimes of magnetic-field annihilation. When a high-intensity laser pulse interacts with a plasma target the accelerated electron bunches generate strong regular magnetic fields [13,14]. A self-generated magnetic field in inhomogeneous near-critical density plasma enhances fast ion generation [15]. It has been predicted that nontrivial topology of self-generated magnetic fields eventually leads to magnetic reconnection [16]. Recent experiments with long nanosecond laser pulses have shown plasma outflows with MeV electrons and plasmoids generated in reconnection current sheets [17,18]. However, the conditions for relativistic magnetic-field line reconnection have not been reached.

In this article, a fast magnetic-field annihilation in relativistic collisionless plasma driven by two collinear ultraintense femtosecond laser pulses is studied with particle-in-cell (PIC) simulations. A significant step with a similar configuration has been done in Ref. [19], where magnetic reconnection occurred at relatively high plasma density and the main contribution to an induced electric field came from electrostatic turbulence and electron pressure according to Ohm's law. In contrast, we demonstrate the magnetic annihilation in low density plasma, when the magnetic-field variation is compensated mainly by the displacement current while the electric current is weak. The induced electric field accelerates charged particles within the current sheet.

II. SIMULATIONS AND RESULTS

The PIC simulations are performed with the relativistic electromagnetic code EPOCH [20], with a 2.5-dimensional configuration (two spatial and three momentum components for particles). A reduced dimensionality here has two advantages. From the physical point of view, it can elucidate the mechanism by removing unnecessary complexity. From the computation side, it is less demanding for computer resources, therefore a larger number of cases with different interaction parameters can be processed to reveal favorable conditions. Two s-polarized Gaussian pulses with the peak intensity of 10^{21} W/cm^2 propagating along the x axis are focused onto the target left edge. Choosing s polarization, we mitigate high frequency laser field effects, facilitating a clear observation of the generated magnetic field and inductive electric field. For each laser pulse the duration is $\tau = 15$ fs and the spot size is 3λ (full width at half maximum), where $\lambda = 2\pi c/\omega = 1\ \mu$m and ω are the laser wavelength and frequency. The optical axes of the laser pulses are at $y = \pm 7\lambda$. This separation guarantees the formation of two independent electron bubbles, not overlapping in a long run. The simulation box size is $195\lambda \times 340\lambda$, large enough to avoid boundary effects. Hydrogen plasma is located in $20\lambda < x < 122\lambda$ with a uniform density along the y axis. The longitudinal density profile is shown in Fig. 1: the density linearly increases from 0 to $0.1n_c$ for $20\lambda < x < 22\lambda$, then remains constant for $22\lambda < x < 62\lambda$, and then linearly decreases to 0 for $62\lambda < x < 122\lambda$. Here $n_c = m_e\omega^2/4\pi e^2$ is the critical density, m_e and e are the electron mass and charge. The transverse size of the target is 40λ. The mesh size is $\delta x = \delta y = \lambda/20$, the quasiparticle number is 10^7 and the

*yanjun.gu@eli-beams.eu

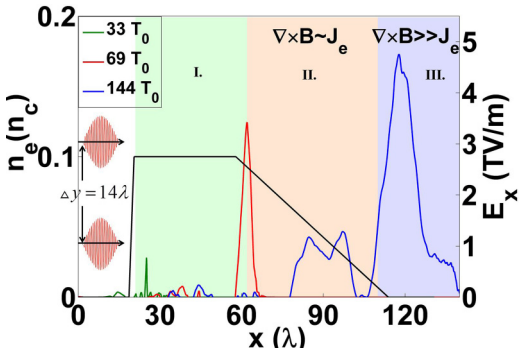

FIG. 1. The electron density (trapezoidal curve) at $t = 0$ and the longitudinal electric field at $33T_0$, $69T_0$, $144T_0$ along $y = 0$; T_0 is the laser period. Zones I, II, and III for the regions of magnetic-field generation, expansion, and annihilation, respectively.

particles are initially at rest. Open boundary conditions are employed for both particles and fields.

The propagation of the laser pulses in plasma results in the formation of two electron bubbles due to the wakefield generation ([21] and references cited therein). The strong wakefields accelerate electrons in the longitudinal direction. According to Ampère's law, the electric currents produce magnetic fields [B_z component in the two-dimensional (2D) case]. The resulting magnetic quadrupole configuration is shown in Fig. 2(a). At this moment, the two magnetic dipoles do not touch each other in the vicinity of the central axis ($y = 0$). The maximum magnetic field can be calculated by using Ampère-Maxwell law, $\nabla \times \mathbf{B} = \mu_0 \mathbf{J_e} + \mu_0 \varepsilon_0 \partial_t \mathbf{E}$.

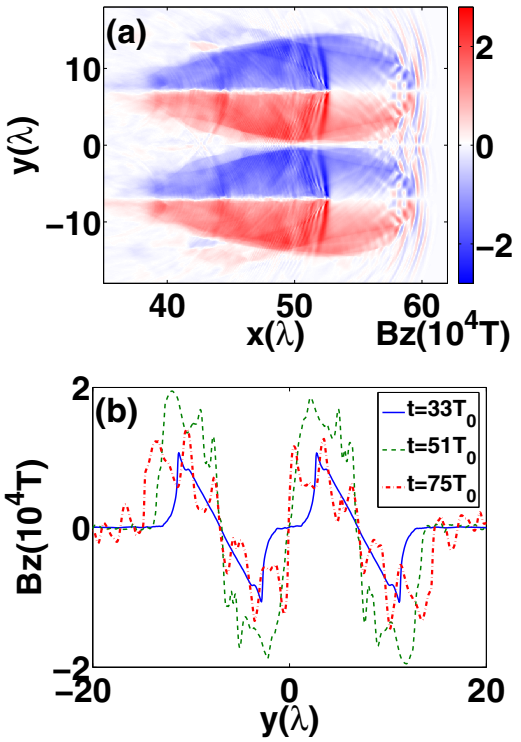

FIG. 2. (a) The magnetic field B_z component at $t = 63T_0$. (b) The expansion of the magnetic dipole: the B_z along $x = 27\lambda$, 40λ, and 68λ at $33T_0$, $51T_0$, and $75T_0$, respectively.

Assuming a quasistatic condition, $\partial_t \mathbf{E} = 0$, we obtain $B/R = \mu_0 n_0 e v_e \approx \mu_0 n_0 e c$, where the electron speed is close to c. The transverse size of the magnetic dipole, R, is estimated to be of the order of $c\sqrt{a_0}/\omega_p$, which is a self-focusing filament radius of a laser pulse with the dimensionless amplitude $a_0 = eE/m_e\omega c$; $\omega_p = (n_0 e^2/\varepsilon_0 m_e)^{1/2}$ is the Langmuir frequency. The magnetic field is then estimated as $B_z = \mu_0 n_0 e c^2 \sqrt{\gamma}/\omega_p$ with the Lorentz factor $\gamma \approx a_0$ [14]. It gives $B_z \approx 1.8 \times 10^4$ T, which is consistent with the simulation result.

When the bubbles reach the density downramp region, where $n(x) = -n_0(x - 122\lambda)/60\lambda$, both the bubble size and the magnetic dipoles expand transversely since the corresponding vortex is affected by a force proportional to $\nabla n \times \Omega$ [22], where Ω is the potential vorticity of electron fluid. Figure 2(b) shows the B_z along $x = 27\lambda$, 40λ, and 68λ at $33T_0$, $51T_0$, and $75T_0$, where $T_0 = 2\pi/\omega_0$ is the laser period. From $33T_0$ to $51T_0$, the quadrupole is propagating in the uniform density region; the displacement between the blue solid peak (for $33T_0$) and the green dashed peak (for $51T_0$) is about 0.3λ. During this stage the magnetic-field strength grows significantly (up to 2×10^4 T), since more electrons are trapped and accelerated by the wakefield. The situation changes when the quadrupole enters the downramp region. The displacement between the green dashed peak and the red dotted peak (for $75T_0$) becomes about 1.6λ. At the same time, the magnetic-field strength slightly decreases, in accordance with Ertel's theorem [23]. The two magnetic dipoles "collide" near the central axis at $y = 0$.

At the central axis the opposite magnetic fields annihilate and the magnetic-field configuration is rearranged, which may be caused by kinklike or/and interchangelike instabilities. Along this axis, a current sheet is formed, where a longitudinal electric field is induced via magnetic-field annihilation. Figure 3(a) shows the longitudinal electric field along $x = 65\lambda$, 80λ, and 90λ at the instants of $t = 81T_0$, $99T_0$, and $123T_0$. At $81T_0$ and $99T_0$, a strong electric field is seen near the laser axes ($y = \pm 7\lambda$). Here the electric field is about 10 GV/cm; the same strength is seen in the case of a single laser pulse. At $t = 123T_0$, the longitudinal electric field becomes much stronger in the current sheet (near $y = 0$) than along the laser axes. The growth of the longitudinal electric field is after the formation and colliding of the magnetic dipoles. This extra contribution comes from the magnetic annihilation which converts the energy of magnetic field to the electric field energy. The magnetic-field distribution at $138T_0$ is shown in Fig. 3(b). In the current sheet region of $100\lambda < x < 110\lambda$, the magnetic quadrupole breaks acquiring a complex structure, in contrast to a smooth distribution behind the breaking region ($x < 100\lambda$). The breaking region indicates that the magnetic fields with opposite directions are annihilating. As a result, a strong longitudinal electric field, E_x, is induced in this region. This is well seen in Fig. 3(c): the green line drawn at the same moment as (b) has the peak ($E_x > 40$ GV/cm) around $110\lambda < x < 115\lambda$. Figure 3(c) also presents the evolution of the longitudinal electric field in the current sheet. The strong inductive electric field moves forward almost with the speed of light.

In order to characterize further the inductive electric field generation, we compare the contributions of different terms in Ampère-Maxwell law. The profiles of $(1/\mu_0)\langle \nabla \times \mathbf{B} \rangle_x$, the

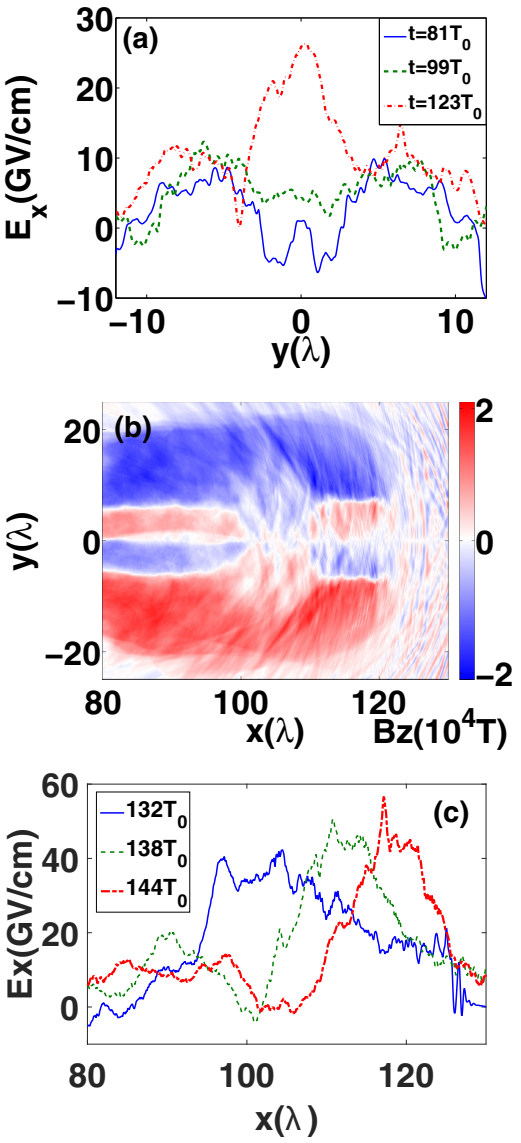

FIG. 3. (a) The inductive longitudinal electric field growth: the E_x along $x = 65\lambda$, 80λ, and 90λ at $t = 81T_0$, $99T_0$, and $123T_0$, respectively. (b) The B_z at $138T_0$. (c) The E_x along $y = 0$ inside the current sheet at $132T_0$, $138T_0$, and $144T_0$, respectively.

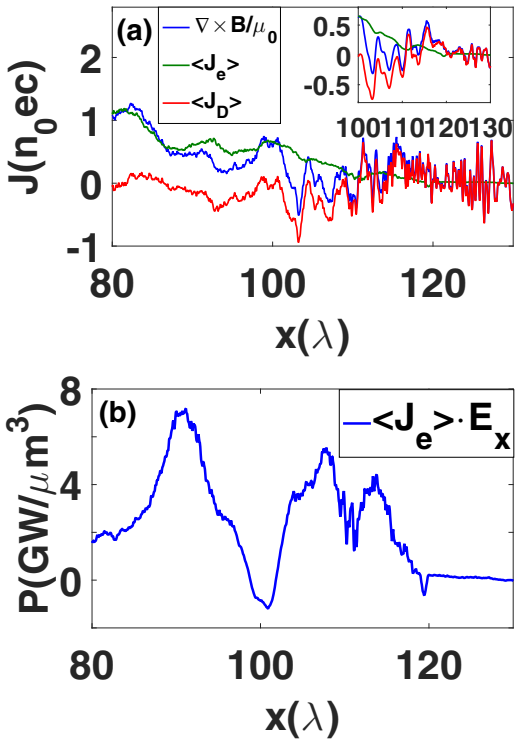

FIG. 4. (a) Contributions of different terms in Ampère-Maxwell law at $138T_0$ along $y = 0$, transversely averaged inside the current sheet ($-\lambda < y < \lambda$). Inset: the same quantities, longitudinally averaged, in the region of the inductive electric field growth. (b) The product $\langle \mathbf{J}_e \rangle \cdot \mathbf{E}_x$ at $138T_0$ along $y = 0$.

electric current density $\langle \mathbf{J}_e \rangle_x = -en\mathbf{v}_x$, and the displacement current density $\langle \mathbf{J}_D \rangle_x = \varepsilon_0 \partial_t E_x$ are shown in Fig. 4(a). $\langle\ \rangle$ denote transverse averaging inside the current sheet ($-\lambda < y < \lambda$). In the region $80\lambda < x < 110\lambda$, return electrons induce a strong electric current. Here $\langle \nabla \times \mathbf{B} \rangle_x$ is sustained by $\langle \mathbf{J}_e \rangle_x$. In the region of $x > 110\lambda$, the electron density becomes low due to the downramp density profile. The variation of magnetic fields can no longer be compensated by the electric current. Therefore, a longitudinal electric field is induced, corresponding to the displacement current which balances the quantity of $\langle \nabla \times \mathbf{B} \rangle_x$. The high frequency oscillations of $\langle \mathbf{J}_D \rangle_x$ agree well with the filaments in magnetic-field distribution. Longitudinally averaged quantities in the inset in Fig. 4(a), where oscillations are smoothed out, show that $\langle \nabla \times \mathbf{B} \rangle_x$ is precisely balanced by the displacement current within the region of the strong inductive electric field. The product $\langle \mathbf{J}_e \rangle \cdot \mathbf{E}_x$ at $138T_0$ along $y = 0$, which is required for the energy conversion between electromagnetic field to particles, is provided in Fig. 4(b). Two peaks can be clearly distinguished, locating at $85\lambda < x < 95\lambda$ and $105\lambda < x < 115\lambda$, respectively. Though both of them are related to magnetic annihilation, the mechanisms are different. For the first peak ($85\lambda < x < 95\lambda$), the current density is rather strong and the electric field is small as seen in Figs. 3(c) and 4(a). This corresponds to the mechanism discussed by Ping *et al.* in Ref. [19] in which the main contribution comes from electrostatic turbulence and electron pressure according to Ohm's law. However, in the second peak ($105\lambda < x < 115\lambda$) where the current density is very low, the magnetic-field annihilation and energy dissipation are based on the mechanism proposed in the above, namely the relativistic collisionless magnetic annihilation. The displacement current grows to compensate the variation of magnetic field and a strong inductive electric field is generated. Therefore, the product $\langle \mathbf{J}_e \rangle \cdot \mathbf{E}_x$ is still large here though the current density is negligible.

The electrons within the current sheet acquire extra energy compared to the electrons at the periphery due to a contribution of the inductive electric field. Figures 5(a) and 5(b) show the distributions of electron longitudinal momentum p_x at $69T_0$ and $138T_0$, which represent the situations without and with the magnetic annihilation effect, respectively. At $t = 69T_0$ the momenta of the electrons within the current sheet ($-2\lambda < y < 2\lambda$) are comparable in magnitude to the momenta of the electrons near the outer wings of laser axis

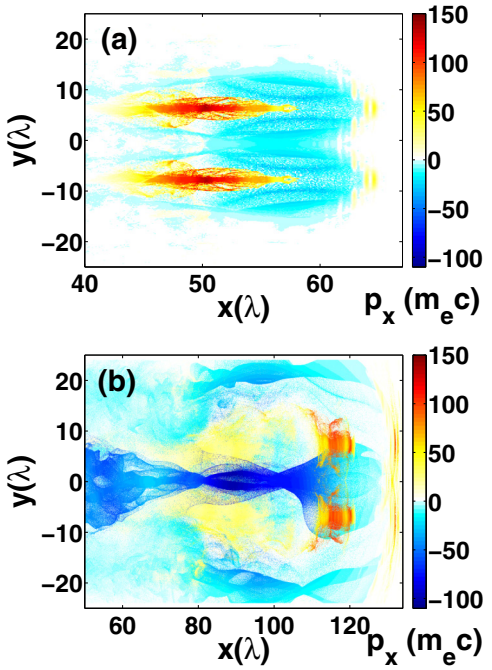

FIG. 5. The electron longitudinal momentum p_x at $69T_0$ (a) and $138T_0$ (b). The figures are plotted by selecting the electrons with maximum energy in each mesh cell.

($8\lambda < y < 25\lambda$ and $-25\lambda < y < -8\lambda$). At this moment p_x distribution is formed by electron oscillations in plasma waves and by the return electrons along the bubble shell. However, at $t = 138T_0$, after the magnetic annihilation came into play, a strong backward accelerated electron bunch appears in the current sheet. The maximum momentum reaches $-120m_ec$, while the momentum growth of the electrons in the wings is not significant. The origin of the backward accelerated electrons corresponds to the emergence of the strong displacement current, i.e., to the inductive electric field as is shown in Fig. 3. Such a strong electron acceleration in the current sheet region is a clear evidence of the magnetic annihilation.

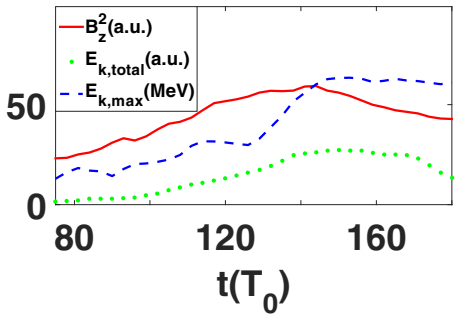

FIG. 6. The evolution of total magnetic-field energy in the simulation box (red line), the total backward electron kinetic energy in the current sheet (green dotted line) and the maximum backward electron energy in the current sheet (blue dashed line) are plotted.

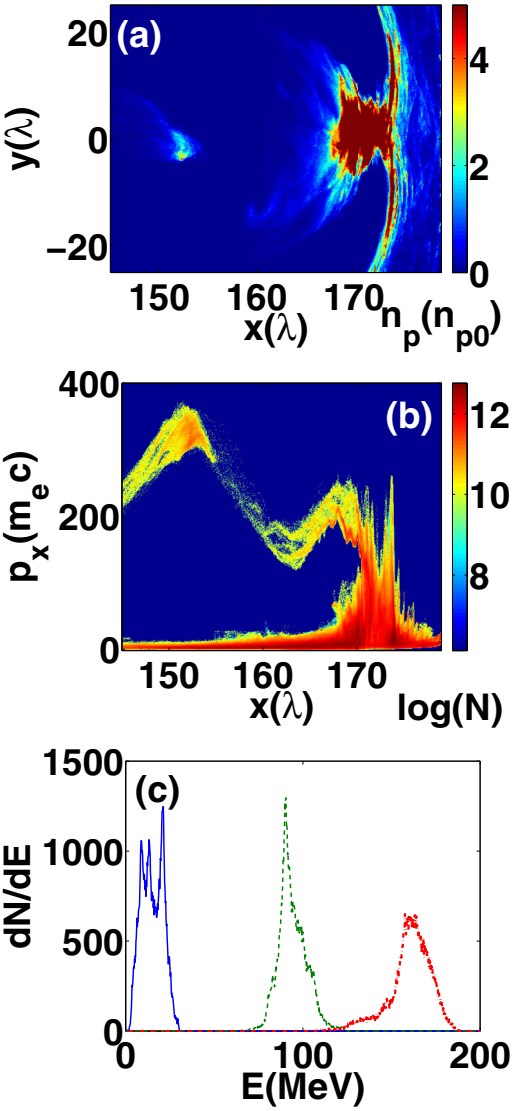

FIG. 7. The positron density (a) and phase distribution in the (x, p_x) plane (b) at $171T_0$; $n_{p0} = 0.01n_c$. (c) The energy spectrum of the positron "bullet" seen in (a) at $150 < x/\lambda < 155$, for $120T_0$, $150T_0$, $180T_0$.

III. ENERGY CONVERSION AND POSITRON ACCELERATION

In order to prove the energy transfer from magnetic field to the backward accelerated electrons, we plot the total magnetic-field energy (B_z^2) in the simulation box, the total electron kinetic energy in the current sheet, and the maximum backward electron energy in Fig. 6. The increase of the total electron kinetic energy (green dotted line) shows that more and more electrons in the current sheet are accelerated. However, the violent rising of the maximum backward electron energy (blue dashed line) indicates that a strong longitudinal inductive electric field is created after $120T_0$, which is consistent with the time when magnetic annihilation occurs based on the previous discussions in Fig. 3(a). The slope of magnetic-field energy in the simulation box (red line) decreases due to the annihilation and energy transfer. The decrease of the total electron energy in the current sheet is because the electrons have transverse

momentum which makes them leave this annihilation region. Furthermore, with the decrease of the electron density as shown in Fig. 1, the electrons which can be accelerated by the inductive electric field become much less. In this case, the acceleration of the electrons in the current is proved to be the effect of magnetic annihilation.

The inductive electric field is sufficiently energetic to be utilized for an efficient charged particles acceleration. Here we consider the case of the positron acceleration, which serves as a diagnostics of a longitudinal electric field created by magnetic annihilation. Positron generation in laser-plasma interactions has been demonstrated in Ref. [24] and the positron acceleration has been discussed by Vieira *et al.* in Ref. [25]. We performed a simulation with the same parameters as above, except that the target now contains positrons, replacing 10% of the protons, and the separation between the laser pulses is enlarged from 14λ to 20λ. With a narrower separation, the current sheet lacks positrons by the time of the magnetic annihilation, because all positrons are swept forward by the laser pulses. When the pulse separation is optimal, a fraction of positrons are squeezed transversely, forming a high density "bullet" within the current sheet between the two bubbles. When the inductive electric field emerges, the positron bullet is accelerated forward up to a high energy. Figure 7(a) shows the positron density distribution at $171T_0$. The high density peak around $x = 170\lambda$ corresponds to positrons directly accelerated by the laser ponderomotive force. Behind, around $x = 150\lambda$, is the high energy positron "bullet" accelerated by the inductive electric field. The bullet maximum momentum is $p_x \approx 350 m_e c$, substantially higher than the momenta of positrons around $x = 170\lambda$, Fig. 7(b). The energy spectrum evolution of the positron bullet is shown in Fig. 7(c). The peak energy increases from 20 to 160 MeV in $60T_0$. At $t = 180T_0$, the positron bullet is quasimonoenergetic with the energy spread of about $\delta E/E \approx 13\%$. Its total charge $\sim$44 pC/μm and its angular divergence is $\sim 14^\circ$. We note that the inductive field more efficiently accelerates positrons forward than electrons backward. This is because the inductive electric field moves forward propagating together with the laser pulses, and thus continuously accelerates positrons. In contrast, the electrons are backward accelerated and quickly leave the region of the inductive field. Although positrons can be accelerated even by single laser pulse with ponderomotive force, the accelerated positrons in that case form a cocoon structure with a quasithermal energy spectrum and large opening angle.

IV. CONCLUSIONS

In conclusion, we identify a regime of collisionless relativistic magnetic annihilation using petawatt femtosecond lasers. In this regime, the variation of $\nabla \times \mathbf{B}$ can only be compensated by the displacement current. When the electric current fails to sustain the magnetic-field gradient due to an insufficient electron density and because the electron velocity is limited by the speed of light, the displacement current emerges. The corresponding longitudinal electric field, induced in the current sheet, accelerates charged particles. In this way the energy of large scale magnetic field is dissipated in a transversely narrow region, being first transferred to electric field and then to the bunches of fast particles. In particular, positrons are accelerated as a quasimonoenergetic bullet in the direction of laser pulses, while electrons are accelerated backward. This provides a signature of this regime for future experiments with petawatt lasers, already operating or upcoming ones such as ELI [26].

ACKNOWLEDGMENTS

This work was supported by ELI (Project No. CZ.1.05/1.1.00/02.0061). Computational resources were provided by the MetaCentrum under the program LM2010005 and by IT4Innovations Centre of Excellence under Projects No. CZ.1.05/1.1.00/02.0070 and No. LM2011033. The EPOCH code was developed as part of the UK EPSRC funded Project No. EP/G054940/1.

[1] D. Biskamp, *Magnetic Reconnections in Plasmas* (Cambridge University Press, Cambridge, England, 2000).
[2] V. S. Berezinskii, S. V. Bulanov, V. L. Ginzburg, V. A. Dogiel, and V. S. Ptuskin, *Astrophysics of Cosmic Rays* (North-Holland/Elsevier, Amsterdam, 1990).
[3] R. B. White, *The Theory of Toroidally Confined Plasmas* (Imperial College Press, London, 2014).
[4] R. G. Giovanelly, Mon. Not. R. Astron. Soc. **107**, 338 (1947); **108**, 163 (1948).
[5] J. W. Dungey, Philos. Mag. **44**, 725 (1953).
[6] J. Birn, A. V. Artemyev, D. N. Baker, M. Echim, M. Hoshino, and L. M. Zelenyi, Space Sci. Rev. **173**, 49 (2012).
[7] E. N. Parker, J. Geophys. Res. **62**, 509 (1957); Astrophys. J. Suppl. **8**, 177 (1963).
[8] P. A. Sweet, in *Electromagnetic Phenomena in Cosmic Physics*, edited by B. Lehnert (Cambridge University Press, London, 1958), p. 123; P. A. Sweet, Nuovo Cimento, Suppl. **8**, 188 (1958).
[9] S. I. Syrovatskii, Sov. Phys. JETP **33**, 933 (1971).
[10] G. W. Inverarity and E. R. Priest, Phys. Plasmas **3**, 3591 (1996).
[11] S. I. Syrovatskii, Sov. Astron. **10**, 270 (1966).
[12] D. Strickland and G. Mourou, Opt. Commun. **56**, 219 (1985).
[13] D. W. Forslund, J. M. Kindel, W. B. Mori, C. Joshi, and J. M. Dawson, Phys. Rev. Lett. **54**, 558 (1985); M. Borghesi, A. J. Mackinnon, R. Gaillard, O. Willi, A. Pukhov, and J. Meyer-ter-Vehn, *ibid.* **80**, 5137 (1998).
[14] G. A. Askar'yan, S. V. Bulanov, F. Pegoraro, and A. M. Pukhov, JETP Lett. **60**, 251 (1994); A. M. Pukhov and J. Meyer-ter-Vehn, Phys. Rev. Lett. **76**, 3975 (1996).
[15] A. V. Kuznetsov, T. Zh. Esirkepov, F. F. Kamenets, and S. V. Bulanov, Plasma Phys. Rep. **27**, 211 (2001); S. V. Bulanov and T. Zh. Esirkepov, Phys. Rev. Lett. **98**, 049503 (2007); A. Yogo, H. Daido, S. V. Bulanov, K. Nemoto, Y. Oishi, T. Nayuki, T. Fujii, K. Ogura, S. Orimo, A. Sagisaka, J.-L. Ma, T. Zh. Esirkepov, M. Mori, M. Nishiuchi, A. S. Pirozhkov, S. Nakamura, A. Noda, H. Nagatomo, T. Kimura, and T. Tajima, Phys. Rev. E **77**, 016401 (2008); Y. Fukuda, A. Ya. Faenov, M. Tampo, T. A. Pikuz, T. Nakamura, M. Kando, Y. Hayashi, A. Yogo, H. Sakaki, T. Kameshima, A. S. Pirozhkov, K. Ogura, M. Mori,

T. Zh. Esirkepov, J. Koga, A. S. Boldarev, V. A. Gasilov, A. I. Magunov, T. Yamauchi, R. Kodama, P. R. Bolton, Y. Kato, T. Tajima, H. Daido, and S. V. Bulanov, Phys. Rev. Lett. **103**, 165002 (2009); S. S. Bulanov, V. Yu. Bychenkov, V. Chvykov, G. Kalinchenko, D. W. Litzenberg, T. Matsuoka, A. G. R. Thomas, L. Willingale, V. Yanovsky, K. Krushelnick, and A. Maksimchuk, Phys. Plasmas **17**, 043105 (2010); T. Nakamura, S. V. Bulanov, T. Zh. Esirkepov, and M. Kando, Phys. Rev. Lett. **105**, 135002 (2010); Y. J. Gu, Z. Zhu, X. F. Li, Q. Yu, S. Huang, F. Zhang, Q. Kong, and S. Kawata, Phys. Plasmas **21**, 063104 (2014).

[16] G. A. Askar'yan, S. V. Bulanov, F. Pegoraro, and A. M. Pukhov, Comments Plasma Phys. Controlled Fusion **17**, 35 (1995).

[17] P. M. Nilson, L. Willingale, M. C. Kaluza, C. Kamperidis, S. Minardi, M. S. Wei, P. Fernandes, M. Notley, S. Bandyopadhyay, M. Sherlock *et al.*, Phys. Rev. Lett. **97**, 255001 (2006); C. K. Li, F. H. Seguin, J. A. Frenje, J. R. Rygg, R. D. Petrasso, R. P. J. Town, O. L. Landen, J. P. Knauer, and V. A. Smalyuk, *ibid.* **99**, 055001 (2007).

[18] J. Zhong, Y. Li, X. Wang, J. Wang, Q. Dong, C. Xiao, S. Wang, X. Liu, L. Zhang, L. An *et al.*, Nat. Phys. **6**, 984 (2010); Q.-L. Dong, S.-J. Wang, Q. M. Lu, C. Huang, D.-W. Yuan, X. Liu, X.-X. Lin, Y.-T. Li, H.-G. Wei, J.-Y. Zhong *et al.*, Phys. Rev. Lett. **108**, 215001 (2012).

[19] Y. L. Ping, J. Y. Zhong, Z. M. Sheng, X. G. Wang, B. Liu, Y. T. Li, X. Q. Yan, X. T. He, J. Zhang, and G. Zhao, Phys. Rev. E **89**, 031101 (2014).

[20] C. P. Ridgers, J. G. Kirk, R. Duclous, T. G. Blackburn, C. S. Brady, K. Bennett, T. D. Arber, and A. R. Bell, J. Comput. Phys. **260**, 273 (2014).

[21] E. Esarey, C. B. Schroeder, and W. P. Leemans, Rev. Mod. Phys. **81**, 1229 (2009).

[22] J. Nycander and M. B. Isichenko, Phys. Fluids B **2**, 2042 (1990); S. K. Yadav, A. Das, and P. Kaw, Phys. Plasmas **15**, 062308 (2008).

[23] V. E. Zakharov and E. A. Kuznetsov, Phys. Usp. **40**, 1087 (1997).

[24] H. Chen, S. C. Wilks, D. D. Meyerhofer, J. Bonlie, C. D. Chen, S. N. Chen, C. Courtois, L. Elberson, G. Gregori, W. Kruer *et al.*, Phys. Rev. Lett. **105**, 015003 (2010); G. Sarri, W. Schumaker, A. Di Piazza, M. Vargas, B. Dromey, M. E. Dieckmann, V. Chvykov, A. Maksimchuk, V. Yanovsky, Z. H. He, B. X. Hou, J. A. Nees, A. G. R. Thomas, C. H. Keitel, M. Zepf, and K. Krushelnick, *ibid.* **110**, 255002 (2013).

[25] J. Vieira and J. T. Mendonca, Phys. Rev. Lett. **112**, 215001 (2014).

[26] *ELI-Extreme Light Infrastructure Science and Technology with Ultra-Intense Lasers WHITEBOOK*, edited by G. A. Mourou, G. Korn, W. Sander, and J. L. Collier (THOSS Media GmbH, Berlin, 2011).